

# Using Caesium-137 to Study Compton Scattering

Alon Shaaltiel, Oren Kereth & Ilan Bessudo

July 24, 2022

## Abstract

Using Cs-137 as a  $\gamma$  radiation source we examine the frequency shift and differential cross section of Compton Scattering. Compton Scattering describes the interaction between a photon and a free electron where the photon deposits only some of its energy. We first scatter the  $\gamma$  rays using an aluminum rod and detect them using a NaI scintillator. We then attempt to reduce background using a trigger mechanism that utilizes a plastic scintillator in place of the aluminum rod.

## Part I

# Introduction

## 1 Interactions of Light & Matter

### 1.1 Cross Section & Differential Cross Section

When describing and identifying an interaction between some target beam and a scattering material an important parameter is the cross section. The cross section,  $\sigma$  is defined for scattering from a single target particle as

$$\sigma = \frac{\text{scattered flux}}{\text{incident flux per unit area}} \quad (1)$$

and so  $\sigma$  is inherently related to the probability of a scatter event and to the rate of scattering events [1]. More accurately, if  $n$  is the density of the scattering particles and  $dP$  is the probability of an interaction in a thickness  $dx$  of material then [1]:

$$dP = \sigma n dx \quad (2)$$

Another useful parameter that gives additional information about an interaction we want to examine is the differential cross section, which is defined as [1]:

$$\frac{d\sigma}{d\Omega} = \frac{\text{flux scattered into element } d\Omega \text{ at angles } \theta, \varphi}{\text{incident flux per unit area}} \quad (3)$$

### 1.2 Photons' Energy Deposition

#### 1.2.1 The Photoelectric Effect

A photon can deposit its entire energy when absorbed by an atomic electron. The photon must have enough energy to either excite the electron to a higher state or to free the electron, thus ionizing the atom. Among the three photon interactions with matter the photoelectric effect is the most dominant at the range of low photon energies (on the order of a few  $KeV$ )[1].

#### 1.2.2 Compton Scattering

One can think of this process as the collision of a photon with energy  $E$  with a free electron at rest, thus delivering some of its energy and momentum to the electron. Unlike the photoelectric effect, the photon does not deposit its entire energy[2]. The energy of the scattered photon,  $E'$ , can be derived using 4-momentum conservation and mass invariance, yielding

$$\frac{1}{E'} = \frac{1}{E} + \frac{1}{m_e}(1 - \cos(\theta)) \quad (4)$$

where  $E$  is the energy of the incoming photon (before scattering off an electron),  $m_e$  is the mass of the electron and  $\theta$  is the scattering angle of the photon [1]. In this experiment we are also interested in the differential cross section of the Compton effect. A classical calculation yields the Thomson differential cross section:

$$\frac{d\sigma}{d\Omega} = r_0^2 \left( \frac{1 + \cos^2(\theta)}{2} \right) \quad (5)$$

where  $r_0 = 2.82 \times 10^{-13} \text{cm}$  is the classical electron radius. A more accurate calculation that takes into account quantum mechanics is known as the Klein-Nishina formula:

$$\frac{d\sigma}{d\Omega} = r_0^2 \frac{1 + \cos^2(\theta)}{2} \frac{1}{[1 + \gamma(1 - \cos(\theta))]^2} \times \left[ 1 + \frac{\gamma^2(1 - \cos(\theta))^2}{(1 + \cos^2(\theta))[1 + \gamma(1 - \cos(\theta))]} \right] \quad (6)$$

where  $\gamma = \frac{E}{m_e}$  [1]. Compton scattering is the most dominant at the mid range energies of below a few MeV [1].

#### 1.2.3 Pair Production

When a photon has sufficient energy, it can be absorbed into the medium and produce an electron-positron (the antiparticle of the electron) pair. This conversion can only occur by having the photon deliver some of its momentum, but very little energy

to nearby nucleus, otherwise momentum-energy conservation is violated. This effect dominates at high energies of a few MeV and higher. [1]

### 1.3 Electrons' Energy Deposit

#### 1.3.1 Ionization

Electrons can ionize atoms in their path by interacting electromagnetically with the bound electrons, thus delivering some of their energy to the newly freed electrons.

#### 1.3.2 Bremsstrahlung

When electrons accelerate or decelerate as a result of electromagnetic interactions with the medium, they emit energy in the form of photons. This form of energy loss becomes dominant in higher energies.

## 2 Radioactive Decays

In this experiment we will be using a radioactive source (Cs-137) that will emit energetic photons in the form of gamma radiation. This section contains a review of beta and gamma decays (excluding alpha decay which is not relevant to this experiment). All radioactive decays are ways through which a nucleus becomes more stable and bound.

### 2.1 Beta Decay

Through the weak interaction, a proton inside the nucleus decays to a neutron, emitting a positron and an electron neutrino [2]. This decay can be expressed as

$${}^A_Z X \rightarrow {}^A_Z Y^{Z-1} + e^+ + \nu_e \quad (7)$$

where  $X$  is the original, less stable nucleus and  $Y$  is the more stable, resulting nucleus of the decay.

### 2.2 Gamma Decay

Similar to how atomic electrons emit photons when de-exciting to a lower energetic level, an excited nucleus can also emit photons by de-exciting, this is a  $\gamma$ -decay. Because the nucleus is more tightly bound (i.e the binding energy is higher than that of the atomic electrons), the emitted photons are much more energetic. An excited nucleus is usually the result of a previous, less stable, nucleus decaying via either  $\alpha$  or  $\beta$  decays. In this experiment the excited Cs-137 is the decay product of Ba-137 which decayed via the emission of a  $\beta$  particle (beta decay).

## Part II

# Experimental Setup & Methods

Throughout all stages of this experiment, some of the equipment used remained unchanged. The equipment and the way it was arranged can be seen in Figure 1

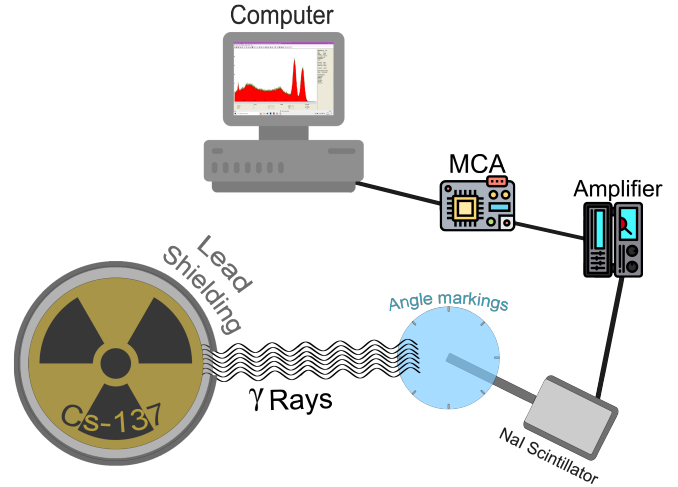


Figure 1: A schematic of the experiment's unchanged equipment

The radioactive source in this experiment is Cs-137, as mentioned in the previous section, it emits  $\gamma$  radiation at a known rate with known energetic values. The source is surrounded by lead shielding that prevents any exposure to radiation, apart from a small slit through which the rays can escape. The  $\gamma$  radiation can be detected by a detector: a NaI scintillator coupled with a photomultiplier tube (PMT). The detector is connected by a rod to the center of a disk with angle markings on its circumference, and its angle can be changed freely. A scintillator is a material that emits detectable light upon the passage of an interacting particle [2]. More concretely, when an incident photon enters the scintillator, it electromagnetically interacts with the medium via the interactions detailed in section 1. These interactions lead to the ionization and excitation of molecules inside the scintillator, followed by more electromagnetic interactions from the ionization electrons and the emission of light from the de-exciting molecules. The avalanche of electromagnetically interacting particles leads to the eventual emission of a somewhat weak, however detectable, light signal (called scintillation light). That scintillation light is detected by the PMT, which amplifies it and converts it into a detectable electric signal. That signal is yet again amplified by an amplifier, whose amplification can be manually controlled and changed. The information is then sent to a Multi Channel Analyzer (MCA), that stores the

signal as a detected count at a certain channel. The number of the channel is proportional to the intensity of the signal delivered to it, which is proportional to the energy of the incident photon (the more energetic it is, the more electrons it ionizes and the larger the avalanche). The MCA then sends the number of counts at each channel to the computer, where a channel histogram can be exported.

### 3 Calibration Setup

A calibration of the system was done at the beginning of the experiment. Two different calibrations were done: an angle calibration and channel calibration. The angle calibration consisted of finding the 0 angle of the Cs-137 source (i.e the center of the beam) relative to which all other angles were measured. This was done by directly measuring (without any scattering medium in between) the flux of  $\gamma$  radiation emitted by the Cs source for small angles around an estimation of the 0 angle. If  $N_0$  is the detected number of  $\gamma$  photons at the 0 angle, denoted by  $\theta_0$ , then for a general angle  $\theta$  the detected number  $N$  is

$$N(\theta) = N_0 \cos^2(\theta - \theta_0) \quad (8)$$

This relation can be shown classically by using the photons wave-like nature. Because the distance between the source and the detector changes with the angle, the measurement for small angles only is justified. For small angles a Taylor expansion of the  $\cos$  function can be done, yielding a parabolic relation for which the angle calibration fit was done

$$N(\theta) = a_0 + a_1\theta + a_2\theta^2 \quad (9)$$

where  $\theta_0$  can be extracted from the maximum of the parabola

$$\theta_0 = -\frac{a_1}{2a_2} \quad (10)$$

Performing the parabolic fit yielded the following graph (see Figure 2)

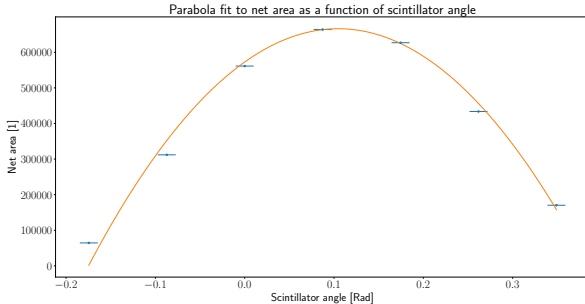


Figure 2: Angle calibration - parabolic fit

with an extracted 0 angle of  $\theta_0 = 0.1048 \pm 0.0080 [rad]$  (7.6%). A calibration between channels and energies is also needed. It is done by placing various  $\gamma$  ray sources with differing energies and identifying the channels they correspond to. These energies

are seen as Gaussian peaks called “photopeaks” at the corresponding channels. The radioactive sources were placed at the center of the disk while the detector was not moved from its place. The center of each photopeak was identified using a Gaussian fit of the form

$$N(x) = \frac{N}{\sigma\sqrt{2\pi}} e^{-\frac{(x-\mu)^2}{2\sigma^2}} + ax + b \quad (11)$$

where  $N(x)$  is the number of counts detected at the channel  $x$ . The linear part of the fit is used to account for background around the photopeak. A linear relation between the photopeak channel,  $C$ , and the photon's energy,  $E$ , was then assumed, and thus a fit of the form

$$E = b_0 C + b_1 \quad (12)$$

was performed. The fit is shown in Figure 3, the fit parameters are shown in Table 1.

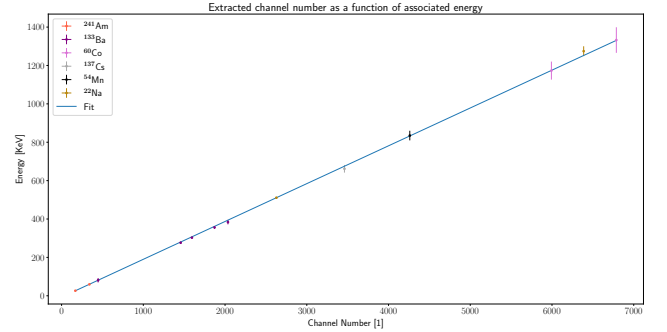


Figure 3: Calibration Fit - Linear fit of energy vs channel number. The fit is in blue and the channel numbers corresponding to the center of the photopeaks of each emission branch of the radioactive sample are in varying colors according to the sample

Fit Parameters	
Parameter	Value (R.E.%)
$b_0 [KeV/Channel]$	$0.19712 \pm 0.00015 (7.6 \times 10^{-2}\%)$
$b_1 [KeV]$	$-7.07 \pm 0.37 (5.2\%)$

Table 1: Fit parameters of the channel-energy calibration fit

Using the same radioactive sources with which the channel calibration was done, the efficiency of the detector for each energy was calculated. The efficiency of the detector,  $\epsilon$ , is defined as

$$\epsilon(E) = \frac{N_{meas}(E)}{N_{in}(E)} \quad (13)$$

where  $N_{meas}(E)$  is the number of counted events in the photopeak corresponding to an energy  $E$ ,  $N_{in}(E)$  is the number of incident photons emitted by the radioactive sources towards the detector. For some of the radioactive sources, there are more than 1 possible emission routes of  $\gamma$  radiation, each with its own energy,  $E$ , and branching ratio, denoted by  $I_\gamma(E)$ .

$N_{in}(E)$  for a radioactive source can therefore be calculated by

$$N_{in}(E) = I_{\gamma}(E) A_0 \frac{S_{det}}{4\pi R_{det}^2} 2^{-\frac{t}{t_{1/2}}} \Delta t \quad (14)$$

Where  $A_0$  is the activity of the radioactive source (i.e the number of decays per second) when the source was first brought to the lab,  $t$  is the time that has passed since then,  $R_{det}$  is the distance between the radioactive source and the detector,  $S_{det}$  is the area of the detector from which incident photons can be detected,  $t_{1/2}$  is the half-life of the source and  $\Delta t$  is the duration of the measurement.  $N_{meas}(E)$  for each photopeak was calculated using the Gaussian fit for that photopeak detailed in equation 11 as it is equal to the parameter  $N$ .  $A_0 2^{-\frac{t}{t_{1/2}}}$  describes the activity of the radioactive source today because the activity is proportional to the number of atoms that have yet to decay, and that number decreases exponentially with a half-lifetime of  $t_{1/2}$ . The data regarding the decays was taken from [3]. A linear fit between the efficiency and the energy of the form

$$\epsilon = c_0 + c_1 E \quad (15)$$

was done. The fit is shown in Figure 4 and the fit parameters and metrics are presented in Table 2.

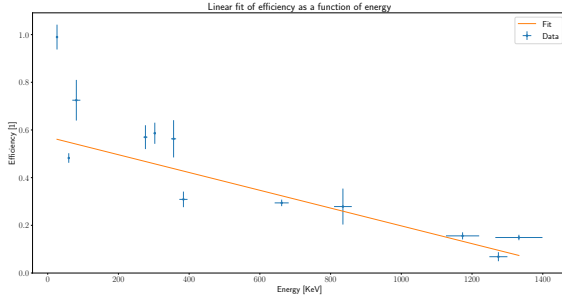


Figure 4: Calculated efficiency as a function of energy.

Efficiency - Fit Parameters	
Parameter	Value (R.E.%)
$c_0$ [1]	$0.571 \pm 0.055$ (9.6%)
$c_1$ [ $10^{-4} \text{KeV}^{-1}$ ]	$-3.73 \pm 0.65$ (17%)
$\chi^2_{red}$	13
$P_{value}$	$4.2 \times 10^{-22}$

Table 2: Fit parameters for the energy-efficiency calibration fit.

As there is no theoretical efficiency relation,  $\chi^2_{red}$  and  $P_{value}$  should only be compared to other fits. In addition, the fit should be as simple as possible because we are trying to generalize. With these two considerations, the linear fit was our best option. It describes the general downward behavior well, however, it crosses 0 efficiency at the 7700<sup>th</sup> channel while the

MCA can get results up to around the 8200<sup>th</sup> channel. Therefore, for higher energies, above the 7000<sup>th</sup> channel, an exponential fit might be better. For our purposes a linear fit is sufficient.

## 4 Compton Scattering from an Aluminum Rod

Upon completion of the calibrations, an aluminum rod was placed at the center of the disk. After placing the rod, the detector started detecting photons emitted by the Cs-137 source that scattered from the aluminum to the detector via Compton scattering. By changing the angle of the detector and identifying the photopeak corresponding to the photons that scattered at that angle (which corresponds to a lower energy, see 4), the energies of the scattered photons were found for different angles. Using this data and the known energy of the  $\gamma$  radiation, the validity of the theoretical model of Compton scattering can be examined as well as that of the Thomson differential cross section and Klein-Nishina's formula detailed in equations 4,5 and 6. The measurements for this part of the experiment and the following one were all made for sufficiently large angles, as at lower angles the photopeak of the photons that scattered once from the rod merges with the photopeak corresponding to photons that reached the detector without passing through the scattering medium. In order to examine the validity of the Thomson and Klein-Nishina models the differential cross section is needed, based on equations 3 and 2 it was estimated as

$$\frac{d\sigma}{d\Omega}(\theta) = \frac{N_{sc}(\theta)/\Omega}{N_{in}n_e l} \quad (16)$$

where  $N_{sc}(\theta)$  is the number of  $\gamma$  rays from the source that have scattered off of the rod at an angle  $\theta$ .  $\Omega$  is the solid angle that the detector covers in the field of view from the rod, meaning  $\Omega = \frac{S_{det}}{R_{Al-det}^2}$  where  $R_{Al-det}$  is the distance between the detector and the rod.  $N_{in}$ , the number of photons that reached the aluminum rod.  $N_{in}$  was calculated via 14 where  $S_{det}$  has been replaced with  $A_{eff}$ , the effective area in the aluminum rod that was exposed to radiation. and  $R_{det}$  has been replaced with  $R_{s-Al}$ , the distance between the source and the rod.  $n_e$  is the density of electrons inside the rod, from which the photons scatter, and  $l$  is the effective distance, defined as  $\frac{V_{eff}}{A_{eff}}$  where  $V_{eff}$  is the volume of the rod that is exposed to radiation. The amount of scattered particles at the angle  $\theta$  was calculated using the detector's sensitivity,  $\epsilon$ , as  $N_{sc} = \frac{N_{meas}(\theta)}{\epsilon(E(\theta))}$  where  $E(\theta)$  is the energy of a  $\gamma$  photon that scattered at angle  $\theta$  and  $N_{meas}$  has been defined previously at equation 13. The use of equation 16 and the length measurements required to use it were carried out in the following part of the experiment, too.

## 5 Compton Scattering from a Plastic Scintillator

In this part of the experiment the aluminum rod was replaced by a plastic scintillator along with some additional equipment, the new setup is presented in Figure 5.

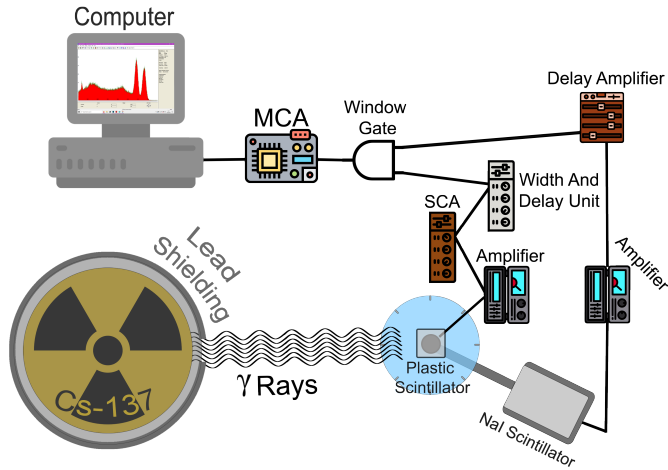


Figure 5: A schematic of the equipment in the second part of the experiment.

The same measurements have been carried out as in the previous setup. The purpose of the added equipment was to reduce the detected background counts that later show up in the histogram. Possible backgrounds can come from photons that have not been scattered by the scattering medium yet were still detected (resulting in another photopeak) as well as photons that have scattered inside the detector and escaped, leaving only a fraction of their energy in the detector. When a photon from the source scatters from the plastic scintillator an electron is freed. The free electron then dissipates its energy inside the scintillator, leading to the emission of scintillation light that is amplified and converted to an electrical signal by a PMT. In the meantime the scattered photon reaches the NaI scintillator where it produces a signal. Both signals are amplified by an amplifier, after which the electron signal reaches the timing Single Channel Analyzer (SCA). The timing SCA checks whether the electron signal is within a set voltage window, otherwise the signal is rejected. From the timing SCA, the signal is sent to the width and delay unit. The purpose of this unit along with the delay amplifier of the photon signal is to synchronize the signals such that they reach the gate at approximately the same time. If two signals reach the gate within a controlled time-frame, the photon signal is sent to the MCA which stores the signal in the appropriate channel. There has to be a causal connection between the electron signal and the photon signal. Therefore, by setting an appropriate voltage window and a time delay for the signal from the detector the background can be greatly reduced.

## Results

### 6 Compton Scattering from an Aluminum Rod

#### 6.1 The Measurements

The measurement is a histogram of events per channel, the histogram is re-binned from 1 channel per bin to 16 channels per bin. A moving average of 3 bins is taken to improve background approximations, but is not used for the final fits. The area between 600 and 4000 channels was chosen as it contains both photopeaks, one from scattered photons and the other from unscattered photons. The area also contains a sample of background before and after the photopeaks which allows background estimation. A linear fit approximates the background and two Gaussian fits estimate the photopeaks as can be seen in Figure 6.

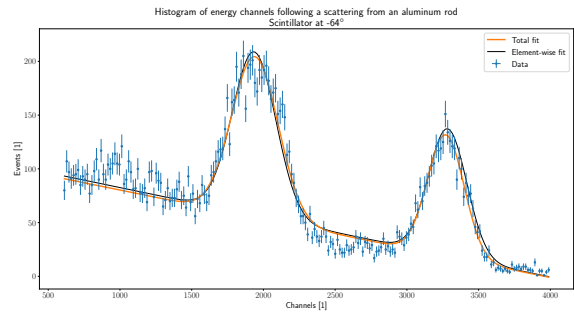


Figure 6: The measured channel histogram after re-binning for aluminum scattering with a scintillator at  $-64^\circ$ . The figure shows a sum of the three separate initial fits for the background and each photopeak (thin black) and a single fit comprising all three (thick orange).

If the two photopeaks are merged, the center and variance of the unscattered photopeak is known from previous fits and its Gaussian can be approximated to help identify the scattered photopeak, Figure 7 shows such an example.



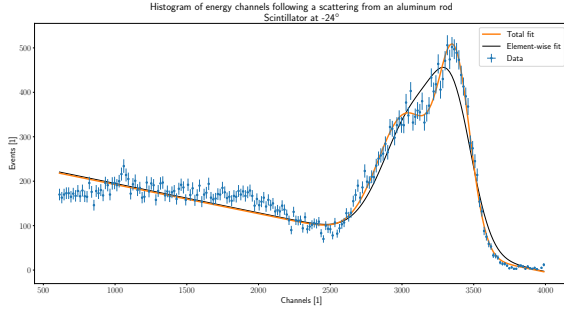


Figure 7: The measured channel histogram after re-binning for aluminum scattering with a scintillator at  $-24^\circ$ . The figure shows a sum of the three separate initial fits for the background and each photopeak (thin black) and a single fit compromising all three (thick orange). Notice how both photopeaks are merged.

## 6.2 Energy-Angle Relation

The detector was placed at different angles and the center of the photopeak corresponding to the photons that scattered from the aluminum rod at that angle was identified. Based on 4 a fit of the form

$$y = d_0 + d_1(1 - \cos(\theta - d_2)) \quad (17)$$

was performed. Where  $y = \frac{1}{E'}$  is the inverse of the estimated scattered photons' energy based on the channel-energy calibration done prior to that.  $\theta$  is the angle of the detector and  $d_i$  are the fit parameters where  $d_0$  is expected to be the inverse of the known energy of the  $\gamma$  rays emitted by Cs-137 taken from [3],  $E_\gamma$ ,  $d_1$  should be consistent with the inverse of the electron mass,  $m_e$ , and  $d_2$  should be consistent with the zero angle that was measured in the calibration. The fit is shown in Figure 8, the fit parameters and the values extracted from them are shown in Tables 3 and 4.

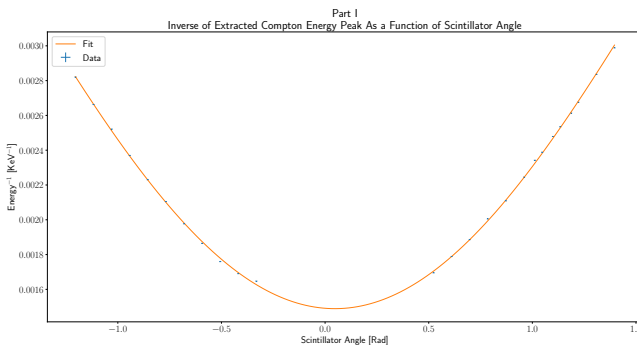


Figure 8: Compton Scattering from an aluminum rod - inverse of the energy vs the angle of the detector fit

Fit Parameters	
Parameter	Value (R.E.%)
$d_0^{Al} [10^{-3}/\text{KeV}]$	$1.4890 \pm 0.0042$ (0.28%)
$d_1^{Al} [10^{-3}/\text{KeV}]$	$1.943 \pm 0.013$ (0.67%)
$d_2^{Al} [\text{rad}]$	$0.0475 \pm 0.0019$ (4.0%)
$\chi_{red}^2$	3.2
$P_{value}$	$4.6 \times 10^{-7}$

Table 3: Compton Scattering from an aluminum rod - fit parameters of the inverse of the energy vs the angle of the detector fit

Extracted Parameters	
Value (R.E.%)	
$E_\gamma = 671.6 \pm 1.9$ (0.28%) [KeV]	
$m_e = 514.7 \pm 3.4$ (0.66%) [KeV]	
$\theta_0 = 0.0475 \pm 0.0019$ (4.0%) [rad]	

Table 4: Compton Scattering from an aluminum rod - extracted parameters of the inverse of the energy vs the angle of the detector fit

$\chi_{red}^2$  and  $P_{value}$  are not in their corresponding desired ranges. A comparison of the extracted values to their theoretical counterparts and the quality of the fit can be found in the Discussion section.

## 6.3 Comparison to Thomson and Klein-Nishina Models

The relation between cross-section and scattering angle is examined.

From the fitted Gaussians to the data,  $N$  (from equation 11) represents the number of counts in the photopeak. Note that re-binning has to be accounted for. From  $N$ ,  $N_{sc}$  is calculated and using equations 14 and 16 the differential cross-section is calculated for each detector angle. Two fits are made, one for the Thomson model shown in 5:

$$y = e_0^2 \cdot \frac{1 + \cos(x - e_1)^2}{2} \quad (18)$$

and the other for the Klein-Nishina model shown in 6:

$$y = f_0^2 \frac{1 + \cos^2(x - f_1)}{2} \frac{1}{[1 + f_2(1 - \cos(x - f_1))]^2} \times \left[ 1 + \frac{f_2^2(1 - \cos(x - f_1))^2}{(1 + \cos^2(x - f_1))[1 + f_2(1 - \cos(x - f_1))]} \right] \quad (19)$$

In both cases,  $y = \frac{d\sigma}{d\Omega}$ , the differential cross-section.  $e_0$  and  $f_0$  are expected to be  $r_0$ ,  $e_1$  and  $f_1$  are expected to be the  $\theta_0$  which was shown in the last section, lastly  $f_2$  is expected to be  $\frac{E_\gamma^{137Cs}}{m_e} = \frac{660}{510}$  [3, 4]. Both fits yielded the following graph (see Figure 9), the fit parameters and metrics are shown in Tables 5 and 6.

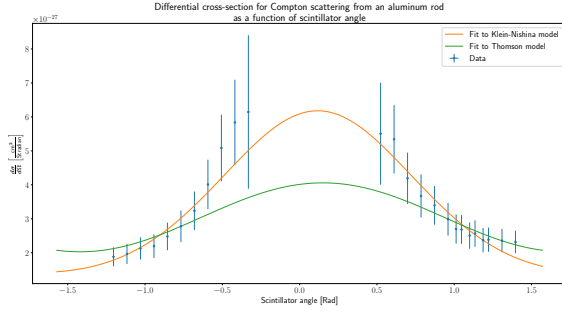


Figure 9: The figure shows the differential cross section of Compton scattering from an aluminum rod as a function of scintillator angle. Two fits are shown, the fit to Thomson model and the fit to the Klein-Nishina model.

Aluminum - Thomson Fit Parameters	
Parameter	Value (R.E.%)
$e_0^{Al} [10^{-14}cm]$	$6.370 \pm 0.099 (1.6\%)$
$e_1^{Al} [rad]$	$0.150 \pm 0.049 (33\%)$
$\chi_{red}^2$	0.81
$P_{value}$	0.71

Table 5: Fit parameters of the fit to the Thomson model presented in 18 for the differential cross-section as a function of scintillator angle.

Aluminum - Klein-Nishina Fit Parameters	
Parameter	Value (R.E.%)
$f_0^{Al} [10^{-14}cm]$	$7.86 \pm 0.31 (3.9\%)$
$f_1^{Al} [rad]$	$0.117 \pm 0.017 (15\%)$
$f_2^{Al} [1]$	$0.58 \pm 0.14 (24\%)$
$\chi_{red}^2$	0.34
$P_{value}$	1.0

Table 6: Fit parameters of the fit to the Klein-Nishina model presented in 19 for the differential cross-section as a function of scintillator angle.

Both models describe the behavior of the data appropriately. The  $P_{value}$  of the Klein-Nishina model is outside our desired range (0.05 to 0.95) while that of the Thomson model is not. The Thomson  $\chi_{red}^2$  is in the desired range while that of the Klein-Nishina model is below it. Both of these results can be attributed to the large uncertainties of the cross-section calculation. These large uncertainties are the result of the merging photopeaks at low angles, shown in Figure 7. The ratios between  $e_0^{Al}$  or  $f_0^{Al}$  with  $r_0$  are  $\frac{r_0^2}{e_0^2} = 2.0 \times 10$  and  $\frac{r_0^2}{f_0^2} = 1.3 \times 10$ , it is likely a factor of 10 is missing in the cross section calculation, as such, our results are an order of magnitude away from the theoretical values. Both  $e_1^{Al}$  and  $f_1^{Al}$  are close to the value presented in the previous section, but have a large uncertainty caused by the large uncertainties in the data.  $f_2^{Al}$  is not very close to the theoretical

value  $\frac{E_{\gamma}^{137Cs}}{m_e} = \frac{662}{511} = 1.3$  and suffers from a large uncertainty. More about the reason for this result and others is presented in the discussion.

## 7 Compton Scattering from a Plastic Scintillator

### 7.1 The Measurements

As was previously stated, the same measurement was taken in this part of the experiment as in the previous, only with less background. The new setup also got rid of the second Gaussian peak, caused by unscattered photons. All we are left with is the scattered peak and a small amount of unavoidable background from the Compton continuum. The most important detail about this background is that it stops slightly before the peak of the photopeak. We approximated it to stop one standard deviation before the mean. We approximated the mean as the maximum and using full width at half maximum, the standard deviation can be approximated. This is all possible because there is no background after the mean. Figure 10 shows the Gaussian approximation, the range after the Compton edge and the Gaussian fit to it.

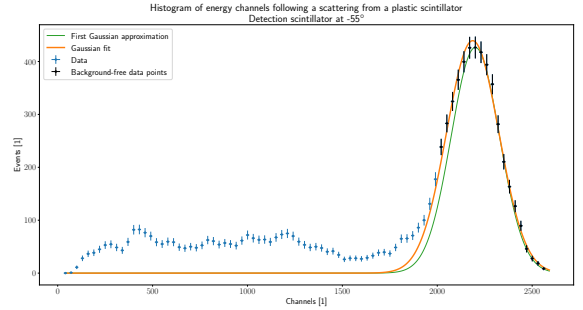


Figure 10: The measured channel histogram after re-binning for scintillator scattering with a detection scintillator at  $-55^\circ$ . The figure shows a Gaussian approximation (thin green line) using points away from the background (black dots) and a Gaussian fit to those points (thick orange line).

Unlike in the previous analysis, here the range of channels is changed for each angle. At the cutoff, there are a hundredth of the maximum event counts. Another change is to the re-binning, the fits were best at 30 channels per bin.

### 7.2 Energy-Angle Relation

The detector was placed at different angles and the fit described in equation 17 was done which has led to the following results (see Figure (11), Tables (7) and 8)

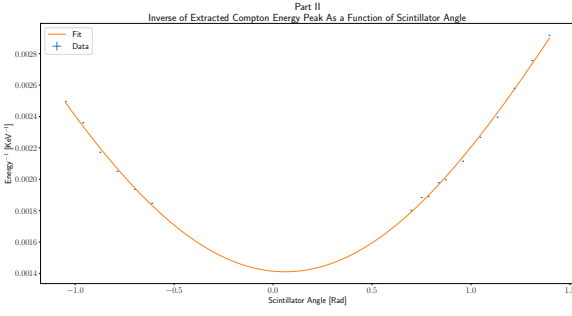


Figure 11: Compton Scattering from a plastic scintillator - inverse of the energy vs the angle of the detector fit

Fit Parameters	
Parameter	Value (R.E.%)
$d_0^{Sci} [10^{-3}/\text{KeV}]$	$1.413 \pm 0.012$ (0.85%)
$d_1^{Sci} [10^{-3}/\text{KeV}]$	$1.927 \pm 0.031$ (1.6%)
$d_2^{Sci} [\text{rad}]$	$0.0614 \pm 0.0034$ (5.5%)
$\chi_{red}^2$	7.1
$P_{value}$	$5.0 \times 10^{-15}$

Table 7: Compton Scattering from a plastic scintillator - fit parameters of the inverse of the energy vs the angle of the detector fit

Extracted Parameters
Value (R.E.%)
$E_\gamma = 707.7 \pm 6.0$ (0.85%) [KeV]
$m_e = 518.9 \pm 8.3$ (1.6%) [KeV]
$\theta_0 = 0.0614 \pm 0.0034$ (5.5%) [rad]

Table 8: Compton Scattering from a plastic scintillator - extracted parameters from the inverse of the energy vs the angle of the detector fit

$\chi_{red}^2$  and  $P_{value}$  are not in their corresponding desired ranges. A comparison of the extracted values to their theoretical counterparts and the quality of the fit can be found in the Discussion section.

### 7.3 Comparison to Thomson and Klein-Nishina Models

Similarly to the last section,  $N$  from the Gaussian fits in equation 11 represents the number of measured scattered counts. This resulted in the differential cross-sections for each angle and the same fits to 18 and 19 are done. The fits are shown in Figure 12 and the fit parameters in Tables 9 and 10.

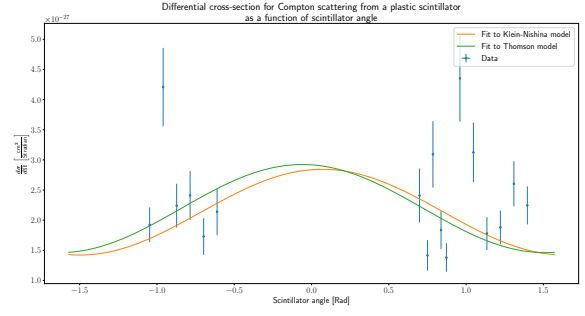


Figure 12: The figure shows the differential cross section of Compton scattering from a plastic scintillator as a function of scintillator angle. Two fits are shown, the fit to Thomson model and the fit to the Klein-Nishina model.

Plastic scintillator - Thomson Fit Parameters	
Parameter	Value (R.E.%)
$e_0^{Sci} [10^{-14} \text{cm}]$	$5.41 \pm 0.25$ (4.6%)
$e_1^{Sci} [\text{rad}]$	$-0.060 \pm 0.148$ (250%)
$\chi_{red}^2$	4.8
$P_{value}$	$2.4 \times 10^{-9}$

Table 9: Fit parameters of the fit to the Thomson model presented in equation 18 for the differential cross-section as a function of scintillator angle.

Plastic scintillator - Klein-Nishina Fit Parameters	
Parameter	Value (R.E.%)
$f_0^{Sci} [10^{-14} \text{cm}]$	$5.33 \pm 0.30$ (5.6%)
$f_1^{Sci} [\text{rad}]$	$0.070 \pm 0.161$ (230%)
$f_2^{Sci} [1]$	$4.3 \times 10^{-7} \pm 1.939086 \times 10^{-2}$ ( $4.5 \times 10^6\%$ )
$\chi_{red}^2$	5.3
$P_{value}$	$3.7 \times 10^{-10}$

Table 10: Fit parameters of the fit to the Klein-Nishina model presented in equation 19 for the differential cross-section as a function of scintillator angle.

As can be clearly seen, neither model fits the data well. The data points seem to be scattered randomly, only the scale is consistent with the previous section. This is also reflected in the fit parameters  $e_1^{Sci}$ ,  $f_1^{Sci}$  and  $f_2^{Sci}$  which all have a relative error above 100%.  $f_2^{Sci}$  is consistent with 0 at this scale, a  $f_2^{Sci}$  of 0 negates the difference between the Klein-Nishina and Thomson models, this again shows that the two are identical for these data points.  $\chi_{red}^2$  and  $P_{value}$  for both fits are well outside the desired ranges. More on the results in the discussion.



## 8 Discussion

### 8.1 First Part of The Experiment

In the first part of the experiment  $\gamma$  rays were scattered by an aluminum rod and were detected by a NaI scintillator that was placed at different angles.

#### 8.1.1 Energy-Angle Relation

The Compton energy-angle relation described by equation 4 was examined. The resulting fit detailed by Figure 8 and Table 3 came out quite well. The fit, as can be seen in the figure, describes the phenomenon adequately. This is also evident from the comparison between the values extracted from the fit parameters and the values in the literature:  $N_\sigma(E_{\gamma_{literature}}, E_{\gamma_{extracted}}) = 0.53$  ( $E_{\gamma_{literature}} = 661 \pm 20[KeV]$  based on [3]) and  $N_\sigma(m_{e_{literature}}, m_{e_{extracted}}) = 1.1$  ( $m_{e_{literature}} = 510.99872804 \pm 0.00000016[KeV]$  based on [4]). Both  $N_\sigma$ s are smaller than 3 standard deviations, the relative errors of the parameters are small, which therefore indicates that the compared values are indeed close. Despite all of that, the statistical values  $\chi_{red}^2$  and  $P_{value}$  are not in their desired ranges.  $\chi_{red}^2$  came out much bigger than 1 and  $P_{value}$  came out smaller than 0.05. This can be attributed to the small errors of all the measurements which can be seen very plainly in Figure 8. Another source for these inadequate statistical values could be the fact that the detector has an angular size  $\delta\theta$ , which means that in each angle  $\theta$  we place the detector we will detect photons that were scattered by an angle in the range  $[\theta - \delta\theta, \theta + \delta\theta]$ . This effect can move the center of the photopeak and lead to slight inaccuracy in the energy measurement. This effect also takes place in the second part of the experiment. Overall, this fit is adequate and allowed for a quite precise measurement of the electron mass and energy of the  $\gamma$  photons. The validity of 17 is consequently confirmed.

#### 8.1.2 Klein-Nishina And Thomson Cross Section Models

Before talking about the fits to the models, we'd like to talk about the scale of  $\frac{d\sigma}{d\Omega}$ , this concerns the second part of the experiment as well. The scale is reflected by  $e_0^2$  and  $f_0^2$ , which are both an order of magnitude smaller than  $r_0^2$ , the exact factor is less relevant, as will be argued later. We believe the missing order of magnitude is due to a wrong constant or wrong units (mm to cm), this is although we have thoroughly checked all units and constants multiple times. This is the most convincing hypothesis as the problem is relevant in both parts of the experiment, even though their analysis is quite different. Now onto the fits, both fits are very good, however, the  $P_{value}$  and  $\chi_{red}^2$  of the Klein-Nishina fit are outside our desired range. This can be attributed to the very large uncertainties at low angles. The reason for these large uncertainties is the photopeak merging shown in Figure 7. The

Eddington python library we use to fit, approximates the fit parameter's uncertainty by changing the parameter's value until the fit is no longer acceptable. If two peaks start to merge, the range of values for  $N$  increases as one peak can "cover" for the other, this is most relevant when the two have merged into a single lob-sided peak (low angles). This argument is in agreement with the uncertainties in the second part of the experiment. This also causes the uncertainty of larger scattering angles to be much smaller than that of small scattering angles. This in-turn flattens the fits as it is better  $\chi^2$ -wise to fit to the tail, as its uncertainty is much smaller. This lessens  $e_0$  and  $f_0$ , which along with the earlier argument, explains their comparison to  $r_0$ . This flattening can also be seen by  $f_2$  as it is smaller than the theoretical value of 1.3. It is likely that the large uncertainties also caused the large relative errors of the fit parameters. Lastly, this uncertainty asymmetry is also responsible for the Thomson model's adequate performance as it can only fit to the tail or the center but not both, but because the center has such high uncertainties it can fit only to the tail and stay statistically relevant. Future analyses could use a different fit parameter uncertainty calculation or ignore the uncertainty caused by the range of possible values.

### 8.2 Second Part of The Experiment

In this part of the experiment the aluminum rod was replaced by a plastic scintillator and new equipment was added to reduce the background.

#### 8.2.1 Energy-Angle Relation

The Compton energy-angle relation was once again examined. The resulting fit detailed by Figure 11 and Table 7 came out well. Just as before the fit seems to describe the phenomenon adequately and the  $N_\sigma$ s turned out smaller than 3, which indicates that the compared values are close to each other as desired:  $N_\sigma(E_{\gamma_{literature}}, E_{\gamma_{extracted}}) = 2.23$  and  $N_\sigma(m_{e_{literature}}, m_{e_{extracted}}) = 0.95$ . Again,  $\chi_{red}^2$  and  $P_{value}$  are not in their desired ranges which can be attributed to the small uncertainty for each of the measurements and to the fact the detector has an angular size as mentioned before.

#### 8.2.2 Klein-Nishina And Thomson Cross Section Models

The fits to both models are well outside the desired  $P_{value}$  and  $\chi_{red}^2$  ranges. Although the data points have the same scale as in the previous part, they seem to be scattered randomly. The reason why they are scattered randomly will be explained later, we'd first like to discuss the fit parameters. As was already stated, the scale, and thus  $e_0$  and  $f_0$  are on par with the last part, as such, their comparison to  $r_0$  is explained.  $f_2$  is consistent with 0 on this scale, thus the two fits are the Thomson model with different initial guesses. We

believe that  $e_1$  and  $f_1$  only reflect our knowledgeable angle measurements. We did not measure close to the center angle and left a gap there. In addition, we measured to around the same negative and positive angle. Both of these choices caused a symmetry in the data around the center angle  $\theta_0$  which is of the same scale as  $e_1$  and  $f_1$  and their uncertainties (ranges). Now onto why the data is random. Unlike the first part of the experiment, there were far less events, and so instead of varying the number of events for each angle we varied the length of measurement. This meant that in equation 16  $N_{sc}$  is now a constant and  $\Delta t$  is the main variable. Our analysis is very focused on calculating  $N$  precisely, while  $\Delta t$  is given directly by the MCA, as such, there may be effects that could not be accounted for. For example, in all measurements the 'live time' outputted by the MCA is two orders of magnitude less than the 'real time'. This is opposed to the first part where the two are almost identical. This suggests that the additional equipment for the second part has affected the performance of the MCA. We would recommend that future studies pick a constant  $\Delta t$ , which would shift the variability to  $N$ .  $\Delta t$

must be sufficiently long to measure large scattering angles, the longest  $\Delta t$  we used is  $360 [sec]$ . An additional improvement can be done to the analysis, by calculating the Compton edge the channel at which the background stops can be found.

## References

- [1] Adrian C. Melissinos and Jim Napolitano. *Experiments In Modern Physics Second Edition*. Academic Press, 2003.
- [2] A. Das and T. Ferbel. *Introduction to Nuclear and Particle Physics Second Edition*. World Scientific, 2003.
- [3] The Lund/LBNL Nuclear Data Search. <http://nucleardata.nuclear.lu.se/toi/index.asp>, 1999. Accessed on 21/7/2022.
- [4] National Institute of Standards and Technology. electron mass- codata value. <https://physics.nist.gov/cgi-bin/cuu/Value?me> Accessed on 17/7/2022.